Journal of Solid State Chemistry **145,** 136–149 (1999)
Article ID jssc.1999.8232, available online at http://www.idealibrary.com on IDEAL®

Irreversible Electron-Induced Structural Change during HREM Imaging in Lithium Ruddlesden–Popper Phases in the Series $Li_2La_x(Nb_{2n-3x}Ti_{3x-n})O_{3n+1}$ ($n = 2, 3, 4$) and $Li_2Sr_{1.5}(Nb_{3-x}Fe_x)O_{10-x}$

M. P. Crosnier-Lopez, N. S. P. Bhuvanesh, H. Duroy, and J. L. Fourquet[1]

Laboratoire des Fluorures, UPRESA 6010 CNRS, Faculté des Sciences, Université du Maine, Avenue O. Messiaen, 72085 Le Mans Cedex 9, France

Received October 12, 1998; in revised form February 14, 1999; accepted February 21, 1999

Several lithium Ruddlesden–Popper compounds are investigated by TEM (ED and HREM) in the series $Li_2La_x(Nb_{2n-3x}Ti_{3x-n})O_{3n+1}$ ($n = 2$, 3, and 4, for $x = 0.833$, 1.78, and 2.25, respectively) and $Li_2Sr_{1.5}(Nb_{3-x}Fe_x)O_{10-x}$ (for $n = 3$; $x = 0$ and 0.115). These studies confirm the crystal structures previously established from single crystal X-ray diffraction data: they consist of perovskite layers separated by Li^+ ions in distorted tetrahedral coordination. After the HREM study, for all the examined compounds, an irreversible structural change is evidenced leading to a unique model (space group *I*4/*mmm*) characterized by the preservation of the perovskite layers and by a substantial shrinking of the *c* parameter (perpendicular to the perovskite slabs). In the hypothesis of the conservation of the cells contents, this phenomenon is explained by a concomitant change in the Li^+ coordination which becomes octahedral.

Key Words: **transmission electron microscopy; lithium containing Ruddlesden–Popper oxides; electron-induced structural change.**

INTRODUCTION

Ruddlesden–Popper (RP) compounds (1) form one of the most important families of layered perovskites owing to various interests such as ion-exchange and intercalation (2–7), ionic conductivity (8, 9), catalysis (10), and ferromagnetic and magnetoresistive properties (11–13). These phases possess a general formula $A'_2[A_{n-1}B_nO_{3n+1}]$, which can be visualized as formed from *n*-perovskite slabs of composition ($A_{n-1}B_nO_{3n+1}$) delimited by the A' atoms (generally Na, K, Rb, Sr, Ca etc.) along the *c* direction and alternate perovskite slabs shifted by $(a + b)/2$. Due to a small difference in the ratio of the various (A', A, and B) cations of various members these compounds are well known to show significant intergrowth structures (14–18). In such situations, X-ray diffraction is a somewhat limited tool for the characterization of these types of materials and electron microscopic study remains an indispensable mean which would clearly indicate the exact nature of the structure. For example, HREM imaging of the layered perovskite $SrNbO_{3.45}$ (19) revealed a quite well-ordered intergrowth of $n = 3$ and $n = 4$ members giving $n = 3.5$.

We have recently reported (20, 21) the synthesis and structural determination, from single crystal X-ray diffraction results, of several phases in the Li–La–Nb–Ti–O and Li–Sr–Nb–Fe–O systems, the structures of which are related to RP phases. Although, the structure of these phases are similar to the RP compounds we find that the *B*-site is partially occupied by the large *A* cations (La or Sr). In this paper we present our electron microscopic (both electron diffraction and high resolution electron imaging) investigations of these phases, which in addition to confirming our results on the X-ray diffraction results, show interesting structural changes in the presence of an electron beam.

EXPERIMENTAL

Synthesis

The crystals and powder samples were prepared as reported in Ref. (20) for the phases $Li_2La_x(Nb_{2n-3x}Ti_{3x-n})O_{3n+1}$ for $n = 2$ ($x = 0.833$) and 4 ($x = 2.25$) members (hereafter, respectively, *n*2 and *n*4) and in Ref. (21) for the phases $Li_2Sr_{1.5}(Nb_{3-x}Fe_x)O_{10-x}$ ($x = 0$ and 0.115) for the $n = 3$ member (hereafter, *n*3); the phase purities of the samples were confirmed from the powder X-ray diffraction patterns (D500 Siemens). For the preparation of samples it is necessary to have a good control of various conditions such as starting composition, temperature, time, intermediate treatments, and cooling rate. For example, our experiments for the preparation of $n = 3$, in the Li–La–Ti–Nb–O system, by heating Li_2CO_3 (Aldrich, purity > 99.99%), La_2O_3 (Johnson Mattey, purity > 99.99%), Nb_2O_5

[1]To whom correspondence should be addressed. Fax: (33) 02 43 83 35 06; E-mail: jlf@fluo.univ-lemans.fr.

0022-4596/99 $30.00

(Aldrich, purity > 99.9%), and TiO_2 (Riedel de Haën, purity > 99.5%) in the molar proportion 2.5 : 0.75 : 0.5 : 2 (with large excess of Li_2CO_3 to act as flux) heated at 1050°C for 6 hr and cooled to room temperature at 1°C/min led to a large number of crystals with a similar morphology. An examination by powder X-ray diffraction shows the simultaneous existence of the three members *n*2, *n*3, and *n*4. Moreover, the crystals were examined in a transmission electron microscope; the electron diffraction as well as high resolution images reveal an intergrowth of the different members indicating their coexistence in the same crystal (Fig. 1). But we could pick single crystals of the *n*3 member in the Li–La–Ti–Nb–O system (of nominal composition $Li_2La_{1.78}(Nb_{0.66}Ti_{2.34})O_{10}$) by heating a mixture Li_2CO_3, La_2O_3, Nb_2O_5, and TiO_2 in the molar proportion 3.75 : 1.5 : 1.0 : 2 at 1050°C for 6 hr and cooling to 60°C at 0.5°C/min. Under our preparation conditions, we did not find phases with *n* higher than 4.

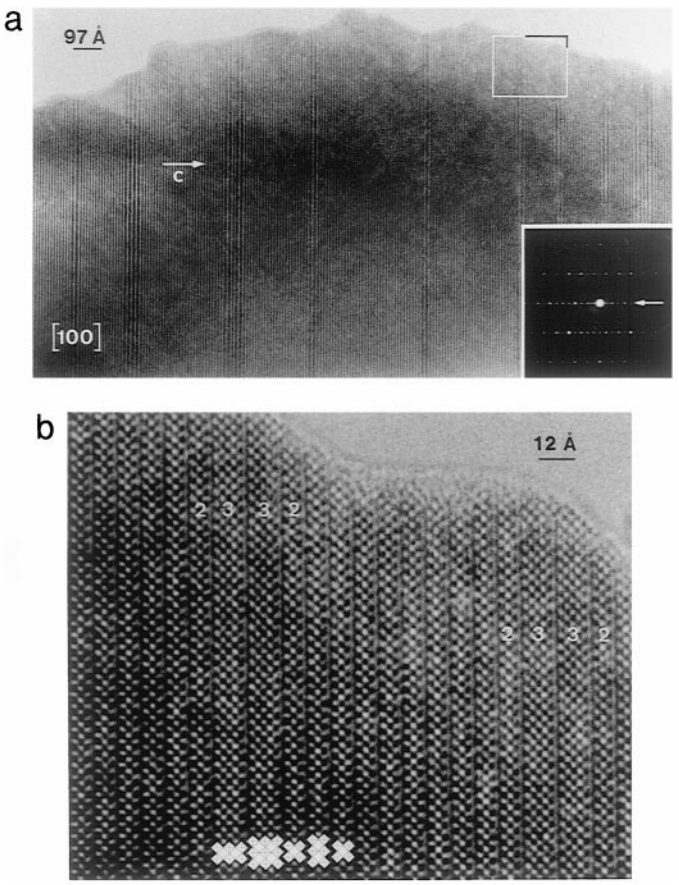

FIG. 1. (a) HREM image along the ⟨100⟩ zone axis showing the simultaneous coexistence of different members and their complete extension through the crystal (SAED pattern with streaks along *c-axis* is given in insert). In (b), an image revealing the existence of a $n = 3$ member in a $n = 2$ matrix is given. The interface between the members corresponds to (010) planes with respect to the structure.

Transmission Electron Microscopy

The transmission electron microscopy (TEM) studies, electron diffraction and high resolution, were carried out with a JEOL 2010 electron microscope operating at 200 kV and equipped with a side entry $\pm 30°$ double tilt specimen holder. Simulations were performed by the multislice method with the EMS programs of Stadelman (22). Images were computed for different thickness and defocus values using the following microscope parameters: spherical aberration constant, Cs = 1.0 nm; defocus spread, $\Delta = 12$ nm; semi-convergence angle, $\alpha = 0.8$ mrad; objective lens aperture diameter, 11.6 nm^{-1}.

For each sample, several crystals were picked and crushed under *n*-butanol in an agate mortar. A drop of the resulting suspension is then placed on a Cu grid covered with a holey carbon film and the grid is allowed to dry before examination in the microscope. EDX analysis was performed on a large number of crystallites with a KEVEX energy dispersive X-ray spectrometer coupled with the TEM. When the results confirm the presence of O, La, Ti, and Nb in the Li–La–Ti–Nb–O compounds and the presence of Sr, Nb, Fe, and O in the Li–Sr–Nb–Fe–O compounds, the accuracy of this method does not allow the exact quantification of the ratio of the various elements present.

RESULTS AND DISCUSSION

Description of the Structure

The structure of the oxides can be characterized by their layers constituted by a cubic arrangement of corner-shared BO_6 octahedra (here, B = Nb, Ti, Fe) with a large A cation (here, La or Sr) partially occupying 12 coordination sites, as found in the perovskite lattice (Fig. 2a). These layers are formed by delimiting the extension of this lattice along one direction and the thickness of each perovskite layer is then given by *n* which determines the number of BO_6 corner-shared octahedra that are connected along the *c* direction perpendicular to the layers. In all these compounds, the stacking of the perovskite layers builds tetrahedral sites delimited by terminal O^{2-} ions and unambiguously filled by Li^+ ions, owing to their small size (Fig. 2b). Although we consider these compounds to be three dimensional, as the distance between the $A_xB_nO_{3n+1}$ slabs are small, the term interlayer spacing is here used to describe the distance between the slabs. The value is obtained from the difference of the *z* coordinate of the two terminal oxygen atoms in adjacent perovskite slabs. We see that, for various compounds in the series, these distances are similar, as one can see from Table 1, and are in good agreement with the value obtained by Sato *et al.* (23). Another point to note is about the BO_6 octahedra: while they are similar and almost regular in all these members, the B atoms of the terminal octahedra occupy always an off-centered position leading to

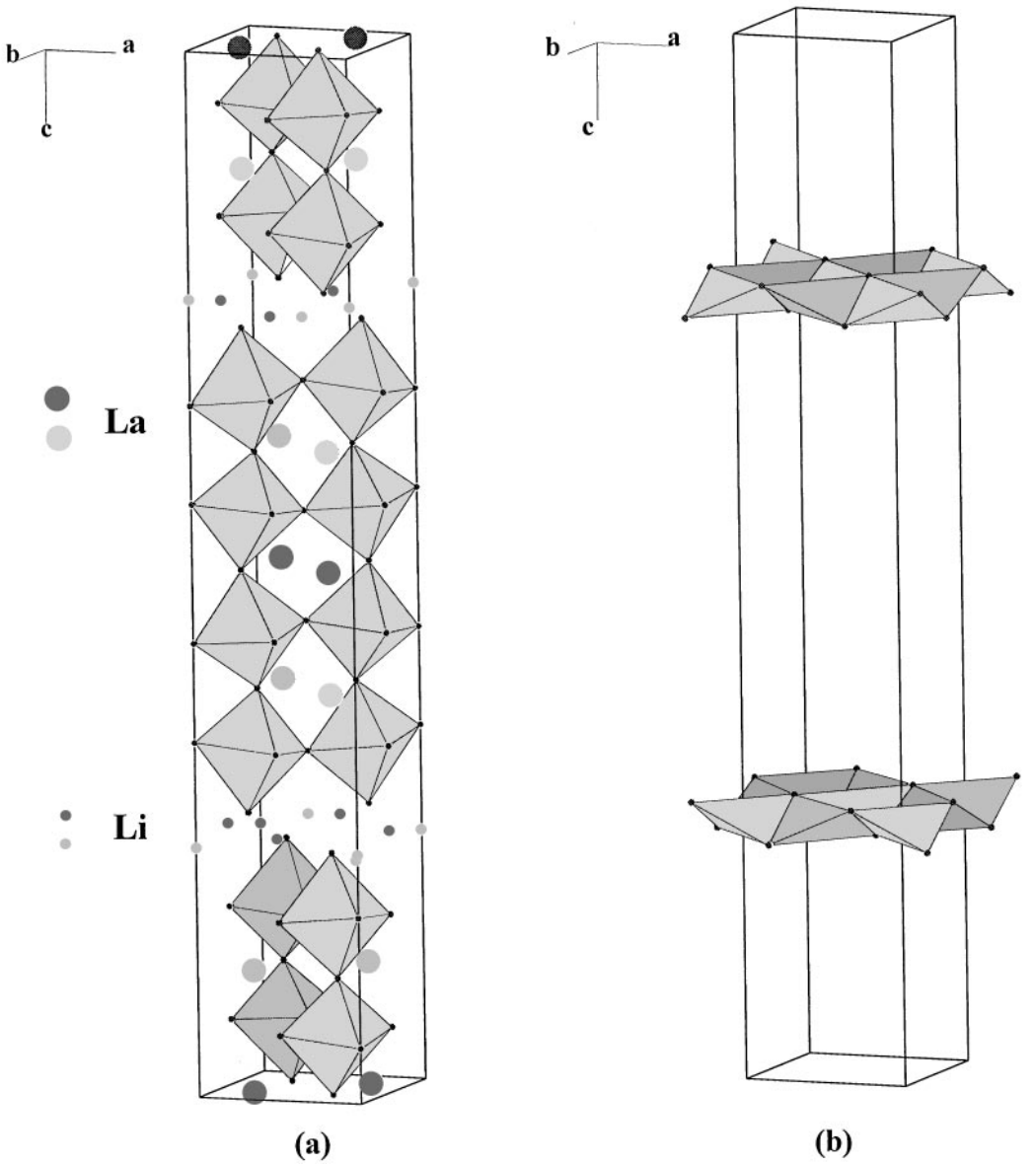

FIG. 2. (a) Perspective view of $Li_2La_{2.25}(Nb_{1.25}Ti_{2.75})O_{13}$ ($n4$) showing the perovskite layers constituted by corner-shared octahedra (Nb, Ti)O_6 and the location of Li^+ ions in the interlayer spacing; (b) Partial view of $Li_2La_{2.25}(Nb_{1.25}Ti_{2.75})O_{13}$ ($n4$) showing the location of the layers of all-vertice-shared LiO_4.

a short terminal *B*–O distance (Table 1), which is well known in layered perovskites (2, 24–27). Finally, while the kinking of the octahedra in all the members of the Li–La–Nb–Ti–O system leads unambiguously to a supercell with $a = \sqrt{2}\, a_p$ (with a_p the parameter of the cubic perovskite-type structure), for the $n3$ (for $x = 0$ and $x = 0.115$) of the $Li_2Sr_{1.5}Nb_{3-x}Fe_xO_{10-x}$ series, the structure can be described in an a_p cell. However, electron diffraction studies in the latter seem to indicate that the real cell would be larger ($a = \sqrt{2}\, a_p$).

Electron Diffraction before HREM Imaging

The electron diffraction (ED) study of each phase is recorded from various crystallites and the reconstitution of their reciprocal space always leads to a tetragonal cell.

Li–La–Ti–Nb–O system—n2 and n4 members. The scan of the reciprocal space allows us to find the cell parameters to be $a = \sqrt{2}\, a_p \approx 5.5$ Å for both members and $c \approx 18.4$ Å for $n2$ and 33.8 Å for $n4$ and to deduce the same

TABLE 1
Unit Cell parameters and Selected Distances for Different Members of the Series $Li_2La_x(Nb_{2n-3x}Ti_{3x-n})O_{3n+1}$ and $Li_2Sr_{1.5}Nb_{3-x}Fe_xO_{10-x}$

n	2	3	3	4
	$Li_2La_{0.833}Nb_{1.5}Ti_{0.5}O_7$ (20)	$Li_2La_{1.78}(Nb_{0.66}Ti_{2.34})O_{10}$ (see text)	$Li_2Sr_{1.5}Nb_{3-x}Fe_xO_{10-x}$ ($x = 0$ and $x = 0.115$) (21)	$Li_2La_{2.25}Nb_{1.25}Ti_{2.75}O_{13}$ (20)
Space group	$P4_2/mnm$ (No. 136)	$P4_2/ncm$ (No. 138)	$I4/mmm$ (No. 139)	$P4_2/mnm$ (No. 136)
a (Å)	5.5334(2) ($\sqrt{2}\,a_p$)	5.47 ($\sqrt{2}\,a_p$)	$x = 0$: 3.953(2) $x = 0.115$: 3.9585(2) (a_p)	5.4915(6) ($\sqrt{2}\,a_p$)
c (Å)	18.3907(2)	26.33	$x = 0$: 26.041(5) $x = 0.115$: 25.915(3)	33.812(4)
Interlayer spacing (Å)	1.36	$\approx$1.3	$x = 0$: 1.16 $x = 0.115$: 1.10	1.22
Li sites	2	2	1	2
Li–O distances (Å)	2.015 and 2.180 for Li1 2.079 for Li2	close to 2.0	$x = 0$: 2.061 $x = 0.115$: 2.054	2.043 and 2.116 for Li1 2.041 for Li2
B sites	1	2	2	2
B–O distances (Å)	1.796 to 2.157	$\approx$1.8 to 2.2 $\approx$1.9	$x = 0$: 1.825 to 2.147 1.932 to 1.996 $x = 0.115$: 1.851 to 2.123	1.803 to 2.203 1.882 to 2.010

P-n extinction symbol for the samples, compatible with the following space groups: $P4_2/mnm$ (No. 136), $P\bar{4}n2$ (No. 118) and $P4_2nm$ (No. 102). Typically, selected area diffraction patterns (SAED) of the [001], [1$\bar{1}$0], and [010] orientations for n4 member are shown in Fig. 3. We observe weak reflections (along the [001]* reciprocal rows, which appear at the extinct positions on the [010] zone axis ED), their intensities being strongly affected by the rotation of the crystal along these directions and hence we attribute these reflections to arise from double diffraction. These results are in good agreement with those obtained by the X-ray diffraction study.

Li–La–Ti–Nb–O system—n3 member. For this compound, while we find the cell parameters to be unquestionably $a = \sqrt{2}\,a_p \approx 5.5$ Å and $c \approx 26.3$ Å, the determination of the real extinction symbol seems to be more difficult. Indeed, the first results[2] related to the X-ray crystal structure determination confirm the cell and suggest an extinction symbol *Pnc* compatible only with the space group $P4_2/ncm$ (No. 138). However, [001] SAED patterns exhibit very weak reflections (shown by arrows, Fig. 4a), which should be absent in the $P4_2/ncm$ space group, while the [010] SAED patterns confirm the c plane (Fig. 4b). Moreover, SAED patterns of some crystallites show diffuse streaks parallel to the c axis which probably indicate a disorder along this direction. The existence of the forbidden reflections on the (001)* plane may be due to double diffraction from the first order Laue zone or may also be due to the presence of (001)-type planar defects which cause streaking parallel to c*. The latter, however, seems unlikely as the intensity of the weak extra reflections are strongly affected by a small tilt in the ab plane.

Li–Sr–Nb–Fe–O system—n3 members. In the case of the compounds $Li_4Sr_3Nb_{5.77}Fe_{0.23}O_{19.77}$ and $Li_4Sr_3Nb_6O_{20}$ a tetragonal cell ($a = a_p \approx 3.9$ Å and $c \approx 26.0$ Å) with body centering is observed (21) (Fig. 5). However, the description of the structure in the $I4/mmm$ space group can be considered as an average structure since SAED patterns of some of the crystallites show diffuse streaks (Fig. 6a) parallel to the c axis indicating a disorder along this direction, their position suggesting a new supercell with $a \approx \sqrt{2}\,a_p$. In one of the crystallites, we even observed distinct weak spots (Fig. 6b) in the [$\bar{1}$10] SAED pattern, leading to the condition $h0l : l = 2n$, corresponding to a c plane. This could be, probably, attributed to a twisting of the middle NbO_6 octahedral layer in the ab plane (21), which is often encountered in related phases (2). Indeed, from the single crystal X-ray

[2] A detailed investigation on the structure determination of this phase will be published elsewhere.

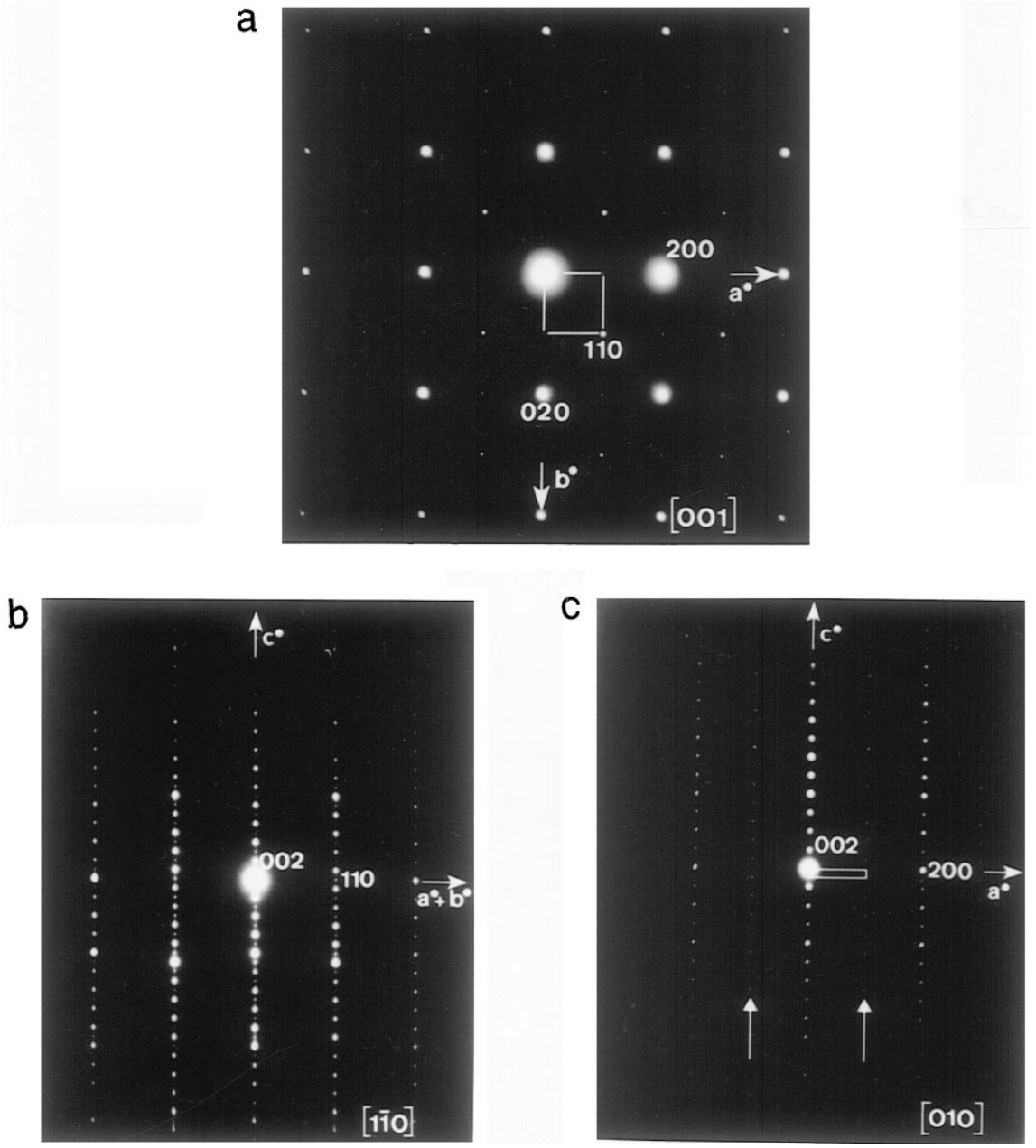

FIG. 3. Three sections of the reciprocal space for $Li_2La_{2.25}(Nb_{1.25}Ti_{2.75})O_{13}$ ($n4$): (a) [001], (b) [1$\bar{1}$0], and (c) [010]. In (c), weak reflections leading to the supercell $\sqrt{2}a_p$ are indicated by arrows.

study, an oxygen atom forming the middle NbO_6 octahedral layer is found to occupy its site with half occupancy and we assume diffuse streaks and distinct weak spots to be due to partial ordering of these sites in some of the crystallites.

High Resolution Electron Microscopy

The [001] high resolution electron microscopy (HREM) image observed on a crystallite of the $n4$ member in the Li–La–Ti–Nb–O system is shown in Fig. 7; it exhibits a contrast classically observed in the perovskite-type oxides: a very regular array of bright dots attesting to the statistical distribution of cations. We have characterized these phases, most often, with the electron beam parallel to the perovskite slabs (along $\langle 110 \rangle$ for the members of Li–La–Ti–Nb–O system and $\langle 100 \rangle$ for $n3$ members of the Li–Sr–Nb–Fe–O system), which gives the best description of the atom stacking of the structure and allows us to see the defects.

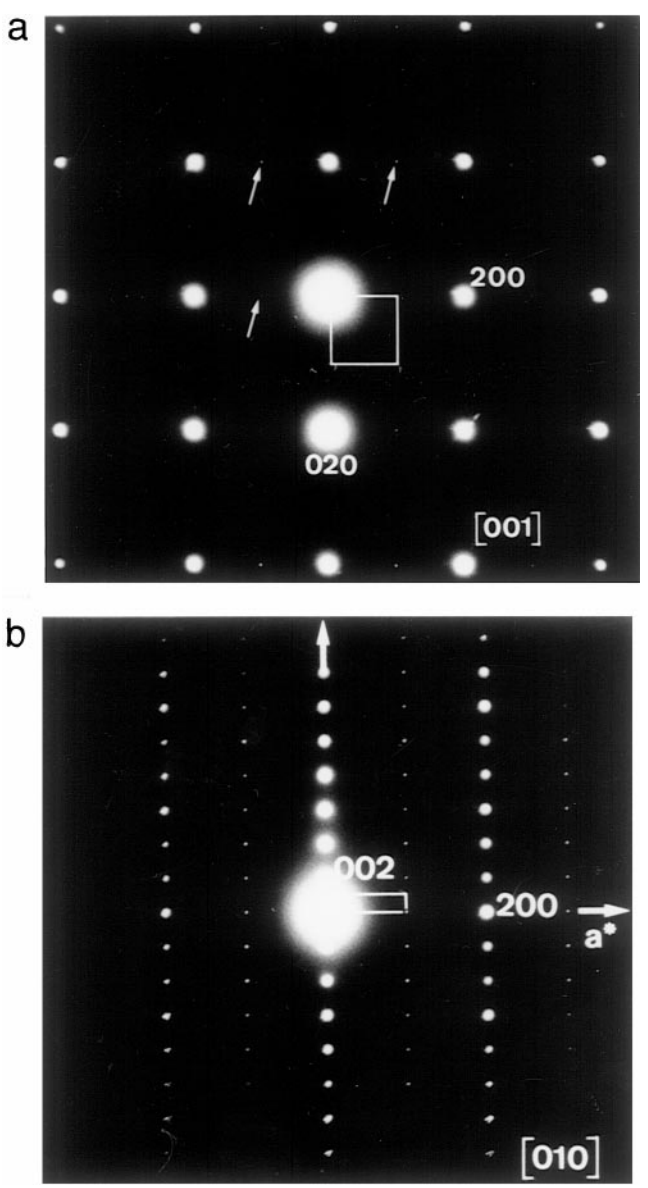

FIG. 4. Two sections of the reciprocal space for $Li_2La_{1.78}(Nb_{0.66}Ti_{2.34})O_{10}$ ($n3$): (a) [001] zone axis showing weak reflections (arrows) forbidden in $P4_2/ncm$ space group, (b) [010] zone axis confirming the c plane.

Typical regular image along ⟨100⟩ observed for $Li_4Sr_3Nb_{5.77}Fe_{0.23}O_{19.77}$ is given in Fig. 8. This characteristic image shows very well the triple octahedral layers alternately shifted by $(a + b)/2$. However, while the interpretation of this image can be directly done without doubt

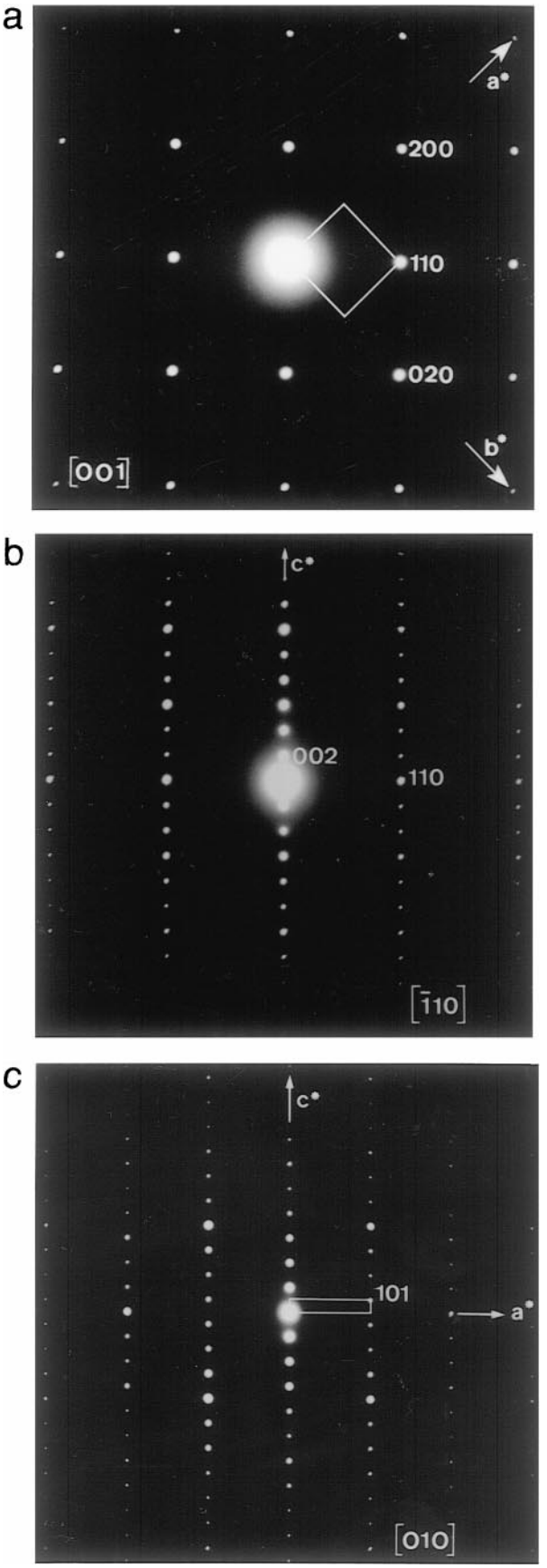

FIG. 5. Typical sections of the reciprocal space of $Li_4Sr_3Nb_{5.77}Fe_{0.23}O_{19.77}$ and $Li_4Sr_3Nb_6O_{20}$: (a) [001], (b) [$\bar{1}$10], and (c) [010] zone axis showing body centered tetragonal cells.

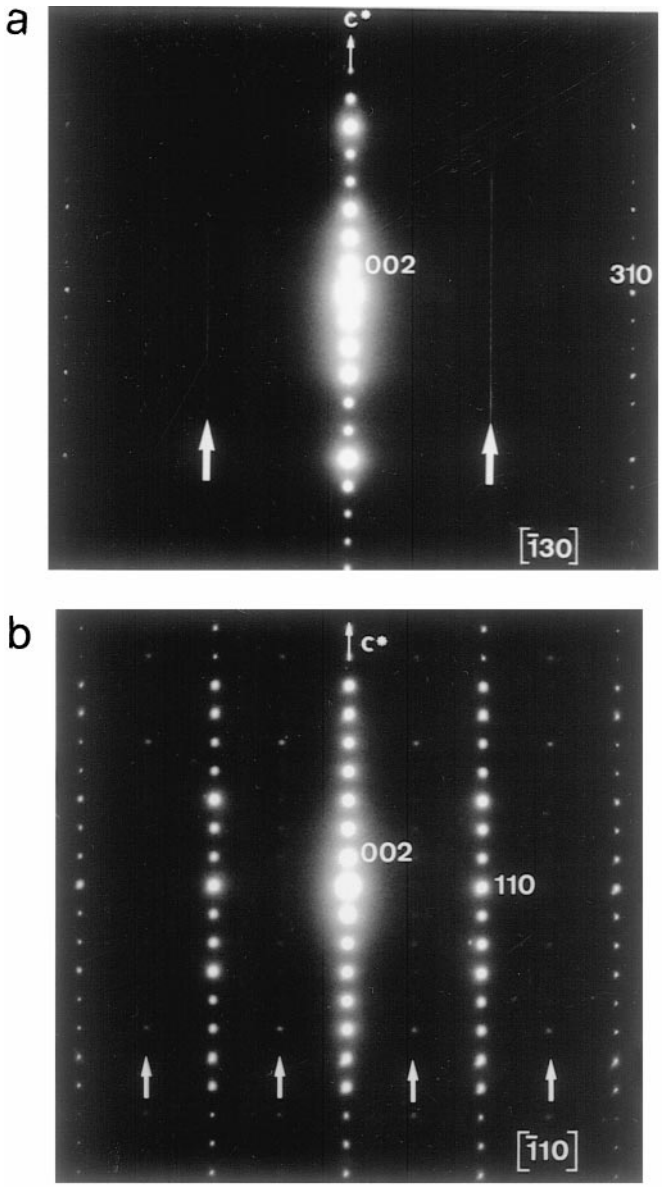

FIG. 6. SAED patterns of $Li_4Sr_3Nb_{5.77}Fe_{0.23}O_{19.77}$ showing (a) diffuse streaks and (b) weak spots leading to a larger a parameter.

by comparison with the projection of the structure along $\langle 100 \rangle$, a careful examination reveals that the periodicity along the c axis is less than that expected (24.9 instead of 25.9 Å, a decrease of about 4%). We show another example for the $n4$ member of the Li–La–Ti–Nb–O system, the HREM image being recorded along the $\langle 110 \rangle$ axis in Fig. 9. Here again we observe that the c parameter is reduced by about 4% (32.4 instead of 33.8 Å).

In order to confirm this observation and to check the other members of the series, similar images are systematically done for all the phases and the SAED patterns of the imaged area are done before and after HREM imaging and

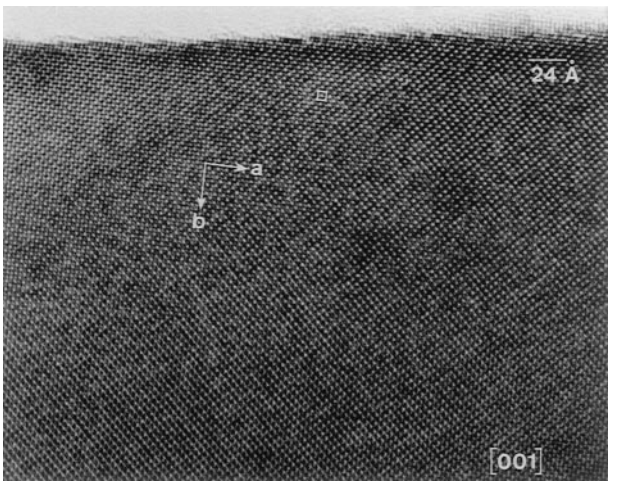

FIG. 7. [001] HREM image observed of $Li_2La_{2.25}(Nb_{1.25}Ti_{2.75})O_{13}$ ($n4$) exhibiting a regular contrast classically observed in the perovskite-type oxides.

a comparison of the two patterns is made. From the results, we see that while there is no significant change in the a parameter, a shrinking of the c parameter is always observed (Table 2). However, for the $n4$ member of the Li–La–Ti–Nb–O system, the c parameter of the final phase is always close to 32.4 Å, whereas for the other phases, the decrease is not always exactly the same. It seems to indicate that the decrease in the c parameter of the cell is a function of the degree of exposition under the beam.

For all the compounds, the position of the reflections in the electron diffraction patterns implies that while the tetragonal symmetry is preserved, an a_p parameter (instead of $\sqrt{2}\,a_p$) must now be used to describe the cell for all the compounds. We give in Fig. 10 the diffraction patterns

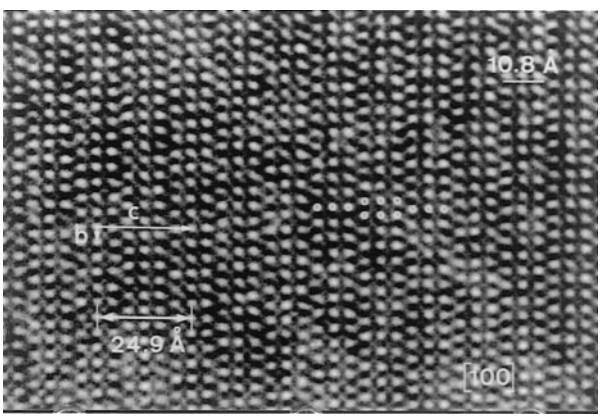

FIG. 8. Typical [100] regular HREM image observed of $Li_4Sr_3Nb_{5.77}Fe_{0.23}O_{19.77}$ ($n3$) showing the triple octahedra slabs shifted by $(a + b)/2$. Note the shrinking of the periodicity along the c axis: 24.9 Å instead of 25.9 Å expected.

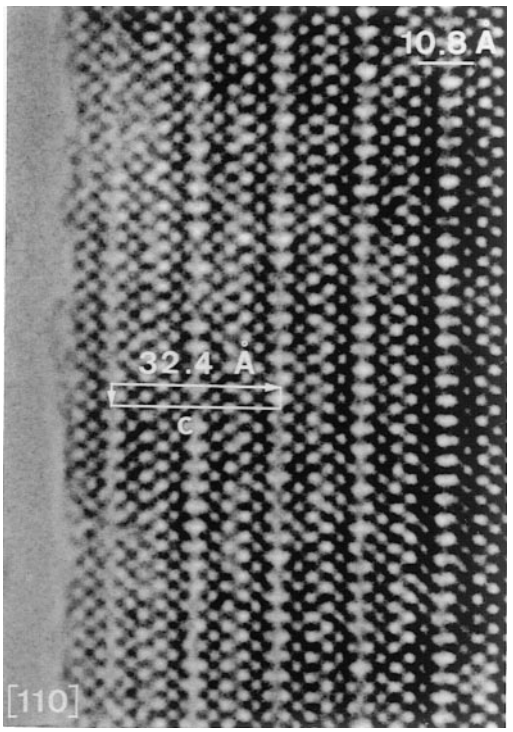

FIG. 9. [110] images observed of $Li_2La_{2.25}(Nb_{1.25}Ti_{2.75})O_{13}$ ($n4$) also revealing a shortening of the c parameter: 32.4 Å instead of 33.8 Å expected.

recorded before and after HREM imaging in the same relative orientations for the $n4$ member: the [100] of the mother structure is parallel to the [110] of the final one while c axes of the two phases are parallel. As one can see, in the [001] zone axis of the mother phase, the reflections $hk0$ with h and/or k odd disappear after HREM imaging whereas reflections with h and k even do not. In the same way, for the [$1\bar{1}0$] and [010] zone axis, the extra weak hkl reflections leading to the supercell $\sqrt{2}\,a_p$ disappear and only the spots corresponding to the tetragonal primitive a_p cell remain with a new limiting reflection condition for hkl, $h + k + l = 2n$, leading to an I-type lattice with two possible Laue classes $4/m$ or $4/mmm$.

At this stage of this study, several remarks must be made about this transformation:

1. We see no gross structural changes before and after HREM imaging except for a shrinking of the c parameter.
2. The process is irreversible. SAED done after 1 month on selected crystallites, already exposed to the beam in HREM, does not reveal the reverse transformation.
3. The conditions used for diffraction allow us to keep the mother phase and were unable to make the transformation. But, the phenomenon occurs immediately under the beam during HREM imaging at a typical magnification of 500×10^3 with an irradiation of the specimen at about 5 A/cm^2.
4. We attempted to prepare the final phase to make a complete X-ray powder study but we could not reproduce the transformation under several conditions outside the microscope. With the intention of testing the influence of high vacuum and the elevation of temperature on the imaged region under the beam, we performed different annealing treatments on the samples: a thermogravimetric analysis coupled with a differential scanning calorimetry (DSC) (TA instruments) was performed under argon at a heating rate of 10°/min up to 1100°C, and heating in a RF coil under secondary vacuum was undertaken up to 1000°C. In order to test the influence of the electron beam on our compounds, we exposed the $n4$ sample, spread on glass plates, to an electron beam scanner (150 kV, 15 mA) in air with

TABLE 2
Evolution of the Cell Parameters for Different Members of the Series $Li_2La_x(Nb_{2n-3x}Ti_{3x-n})O_{3n+1}$ and $Li_2Sr_{1.5}Nb_{3-x}Fe_xO_{10-x}$ after HREM Imaging

n	2	3	3	4
	$Li_2La_{0.833}Nb_{1.5}Ti_{0.5}O_7$ (20)	$Li_2La_{1.78}(Nb_{0.66}Ti_{2.34})O_{10}$	$Li_2Sr_{1.5}Nb_3O_{10}$ (21)	$Li_2La_{2.25}Nb_{1.25}Ti_{2.75}O_{13}$ (20)
		Before HREM imaging		
Space group	$P4_2/mnm$	$P4_2/ncm$	$I4/mmm$	$P4_2/mnm$
a (Å)	5.53	5.47	3.95	5.49
c (Å)	18.39	26.33	26.04	33.81
Interlayer spacing (Å)	1.36	≈1.3	1.16	1.22
		After HREM imaging		
Space Group	$I4/mmm$	$I4/mmm$	$I4/mmm$	$I4/mmm$
a (Å)	3.9	3.9	3.9	3.9
c (Å)	16.7 to 17.7	24.1 to 24.6	24.6 to 25.1	32.4
Δc (Å)	−1.4 (mean)	−1.9 (mean)	−1.1 (mean)	−1.4

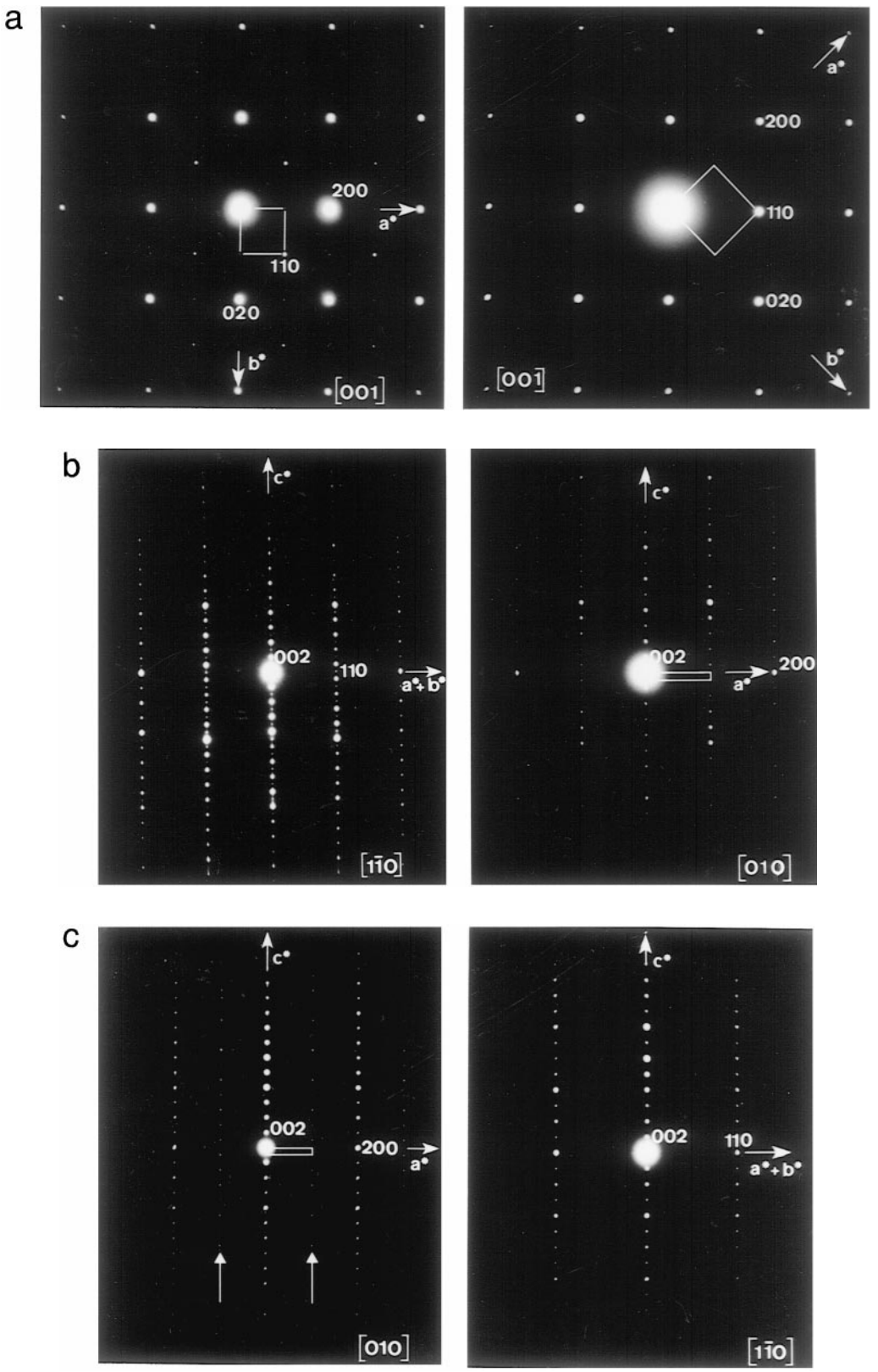

FIG. 10. SAED patterns of $Li_2La_{2.25}(Nb_{1.25}Ti_{2.75})O_{13}$ ($n4$) of the same crystallites before and after HREM imaging in the same relative orientations: (a) [001], (b) [1$\bar{1}$0], and (c) [010] zone axis of the mother phase (on the left). The irreversible transformation after HREM imaging involves a decrease of the c parameter and a change in the space group ($P4_2/mnm$ to $I4/mmm$) with tetragonal symmetry being preserved.

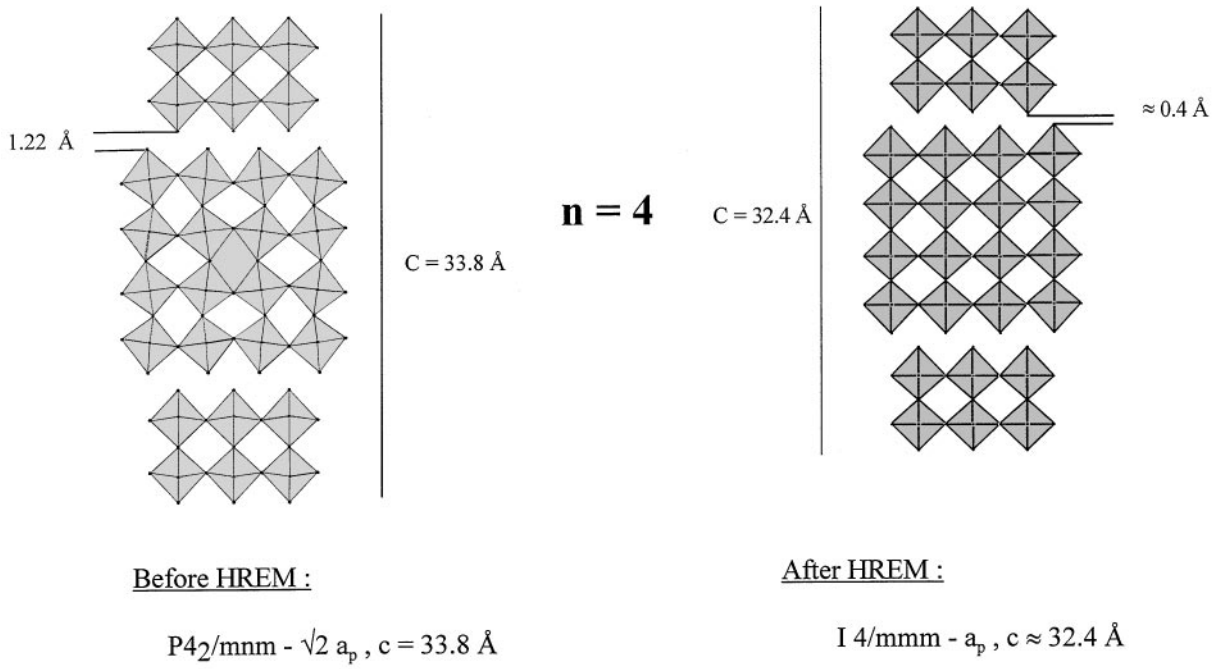

FIG. 11. Schematic drawings for $Li_2La_{2.25}(Nb_{1.25}Ti_{2.75})O_{13}$ ($n4$) of the perovskite slabs before and after HREM: the transformation is here assumed to be due to a straightening of the puckered octahedra of the perovskite layers with a lowering of the interlayer spacing from 1.22 to 0.4 Å (the *B*–O distances kept constant).

successive exposures of 50 kgy dose (with a maximum of 150 kgy) at the rate of 24 m/min. Under our conditions, powder X-ray diffraction patterns of the resulting phases did not show any shrinking of the *c* parameter.

5. The decrease in the *c* axis, observed on various members, seems to be independent of the *n*-values (Table 2).

The capability of following solid-state reactions *in situ* during high-resolution electron microscopic investigations is well known (28, 29). However, in some cases, it seems that HREM imaging induces a reaction which would not occur without the effect of direct electron beam irradiation (30): oxidation, reduction, synthesis, or decomposition have been observed *in situ* and would not have happened in vacuum at any reasonable temperature caused by the beam required for observation. In other cases, on the contrary, the transformations that occur under an electron beam could be due to heating of the samples (31) (e.g., dehydration).

We could propose three possible reasons to explain this observed transformation.

The first one should be due to a departure of Li_2O caused by the increase in temperature of the imaged region under the beam, creating oxygen vacancies. Layered perovskites are well known to exhibit oxygen vacancies (32, 33). In such a case, the shortening observed in the *c* parameter is in disagreement with at least two studies on compounds, the crystal structures of which are related to that of the Ruddlesden–Popper phases. Sato *et al.* (23), have shown that the Li intercalation in $LiLaNb_2O_7$, yielding $Li_2LaNb_2O_7$,

TABLE 3

Fractional Atomic Coordinates and Main Interatomic Distances for $Li_2La_{2.25}(Nb_{1.25}Ti_{2.75})O_{13}$ ($n4$) after HREM Imaging (Obtained from the Proposed Model)

Space group: *I*4/*mmm* (139)
$a \approx a_p \approx 3.88$ Å and $c \approx 32.4$ Å; $V \approx 487.8$ Å^3
$Z = 2$; formula weight (g): 782.31
D_{calc} (g/cm^3) ≈ 5.3
Interlayer spacing ≈ 0.4 Å

Atom	site	*x*	*y*	*z*
(Nb/Ti)1	4e	0	0	0.188
(Nb/Ti)2	4e	0	0	0.058
La1	2b	0.5	0.5	0
La2	4e	0.5	0.5	0.123
O1	4e	0	0	0.244
O2	8g	0.5	0	0.188
O3	4e	0	0	0.120
O4	8g	0.5	0	0.058
O5	2a	0	0	0
Li	4d	0.5	0	0.25

Selected interatomic distances
LiO_6 octahedra
Li–O2: 2 × 2.01 Å
Li–O1: 4 × 1.95 Å
(Nb/Ti)1O_6 octahedra
(Nb/Ti)1–O1: 1.80 Å
(Nb/Ti)1–O2: 4 × 1.94 Å
(Nb/Ti)1–O3: 2.20 Å
(Nb/Ti)2O_6 octahedra:
(Nb/Ti)2–O5: 1.88 Å
(Nb/Ti)2–O4: 4 × 1.94 Å
(Nb/Ti)2–O3: 2.01 Å

results in a decrease in the c parameter ($c = 20.361$ Å for $LiLaNb_2O_7$ and $c = 18.633$ Å for $Li_2LaNb_2O_7$) and in turn a decrease in the interlayer spacing (2.20 to 1.29 Å) with a shortening of the Li–O distances (2.33 Å in $LiLaNb_2O_7$ to 2.07 Å in $Li_2LaNb_2O_7$). Moreover, the study realized by Lee *et al.* (32), about oxygen stoichiometry, shows that an oxygen departure would result in an increase of the c parameter: the reversible intercalation of oxygen in the phase $LaSr_3Fe_3O_{10-\delta}$ and in the mixed Fe/Al analogue, for which the crystal structure consists of a triple layer of octahedra ($n3$) separated by La/Sr–O layers, reveals that the value of the c parameter is a linear function of the oxygen stoichiometry. The c parameter increases with decreasing oxygen content and it varies from 28.04 Å for the phase $LaSr_3Fe_3O_{9.9}$ to 28.52 Å for the phase containing 9.2 oxygen atoms. Thus, under such conditions, the hypothesis of Li_2O volatilization seems very unlikely.

The second possibility to explain the shortening of the c parameter concerns an increase of the tilting of the octahedra. However, this solution must be rejected because it is inconsistent with the $I4/mmm$ space group observed for the final phase and would lead to too short interatomic distances (A–O in $A'_2[A_xB_nO_{3n+1}]$).

A third hypothesis, which is most likely for the observed changes, is the straightening of the puckered perovskite slabs accompanied by a lowering of the interlayer spacing (Fig. 11). Many structural works have been done on Ruddlesden–Popper related phases, but most of these studies have been performed only with powder X-ray or neutron diffraction data (1, 2, 23, 24, 34, 35). The X-ray structural refinements are often realized in the $I4/mmm$ space group, leading to an average structure, whereas TEM studies and neutron diffraction data clearly show superlattice reflections involving a larger cell (2, 3). In our case, for the three members of the Li–La–Nb–Ti–O system, the cell of the mother phase is found unambiguously tetragonal with $a = \sqrt{2}\,a_p$ and the anionic displacements lead to a tilt of the octahedra making puckered perovskite layers (Table 1). During the transformation, under the beam, the cell becomes simpler ($a = a_p$), and we can imagine that it is due to a straightening up of the octahedra. In fact, if we assume this hypothesis, in the $I4/mmm$ space group, with the same

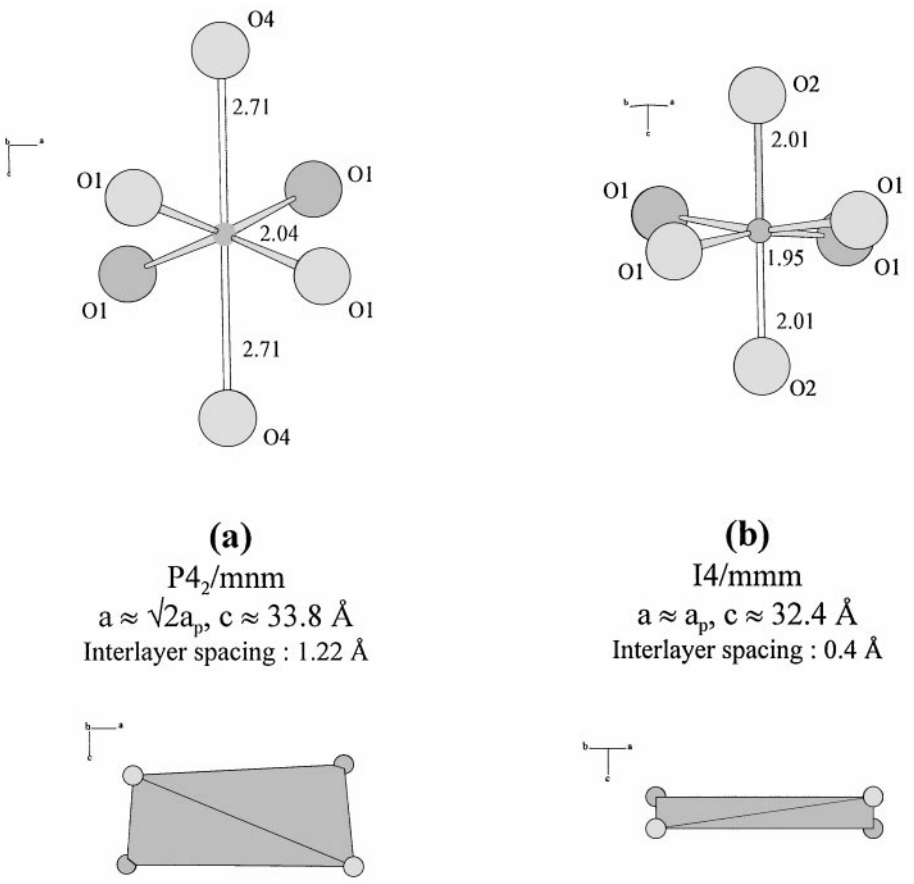

FIG. 12. Schematic drawings for $Li_2La_{2.25}(Nb_{1.25}Ti_{2.75})O_{13}$ ($n4$) of the oxygen environment evolution around Li^+ ions during the transformation under the beam in HREM: (a) in the mother phase, a tetrahedral coordination is observed; (b) after HREM observation, the approach of the two apical oxygen leads to a new octahedral coordination. In the lower part of the figure, the evolution of the tetrahedra is shown.

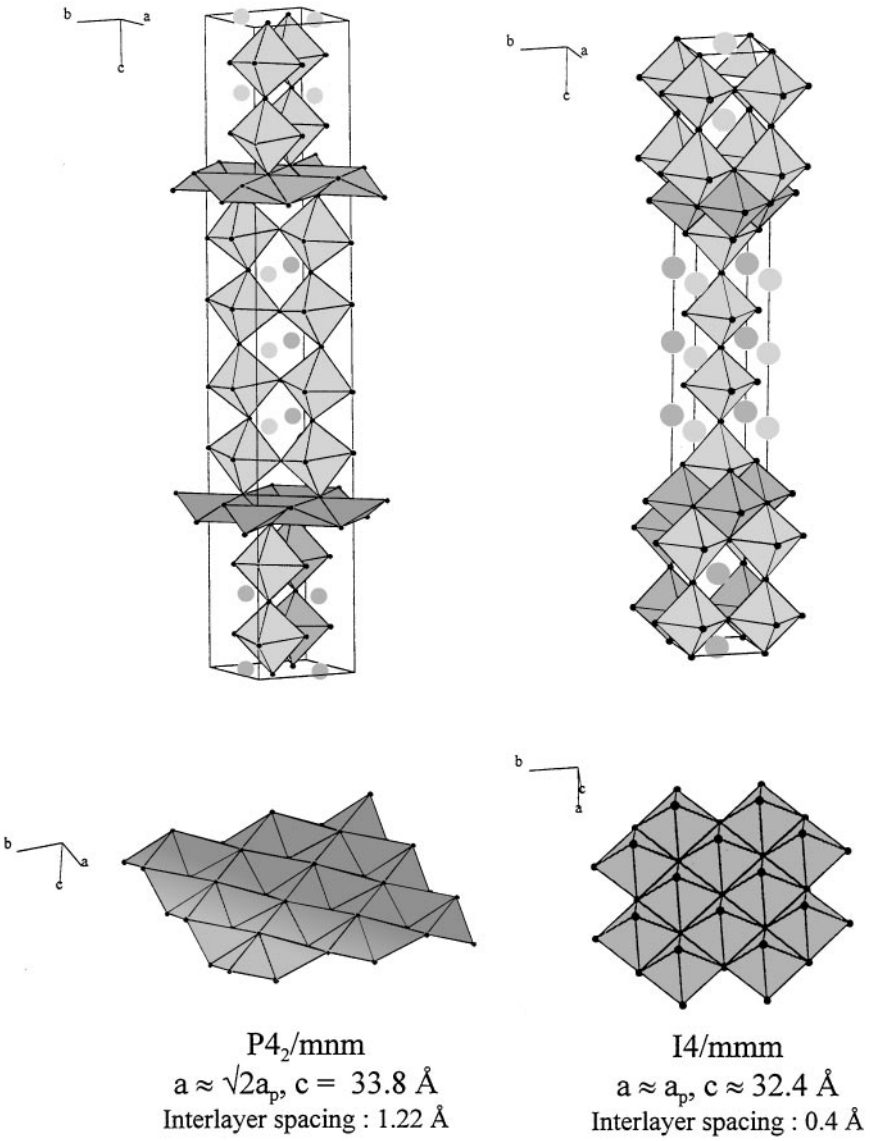

FIG. 13. Idealized drawings for $Li_2La_{2.25}(Nb_{1.25}Ti_{2.75})O_{13}$ ($n4$) of the two structures before and after HREM showing the transformation of the Li^+ environment under the beam.

observed *B*–O distances in the mother phase, it is possible to deduce approximately the positional parameters for the atoms and to see the evolution of the interlayer spacing and of the Li–O distances.

We have made such calculations in the case of $Li_2La_{2.25}(Nb_{1.25}Ti_{2.75})O_{13}$ ($n4$). The cell parameters of the final phase are $a \approx 3.9$ Å and $c \approx 32.4$ Å as found in electron diffraction. Under these conditions, the calculated fractional atomic coordinates are given in Table 3 with the main interatomic distances. It must be pointed out that the calculated Li–O distances are in agreement with values observed for Li–O octahedra (36–40) with a small interlayer spacing (0.4 Å in the final phase compared to 1.22 Å in the mother phase). However, the most important point to be noted is the modification of the Li environment: in the mother phase, a distorted tetrahedral coordination is observed, while in the final one, two other oxygen atoms (O4) approach Li (Li–O distances being now 2.0 Å instead of 2.7 Å) and must be considered now in its direct environment, leading to a new octahedral coordination (Figs. 12a and 12b) with normal Li–O distances. Further contraction along the *c* axis is unlikely. The two structures ($c = 33.8$ Å and $c = 32.4$ Å) are drawn in Fig. 13. In the mother phases, the terminal O^{2-} ions of the perovskite slab build tetrahedral sites occupied by Li^+ ions, constituting layers parallel to the (001) plane of all-vertice-shared tetrahedra. In

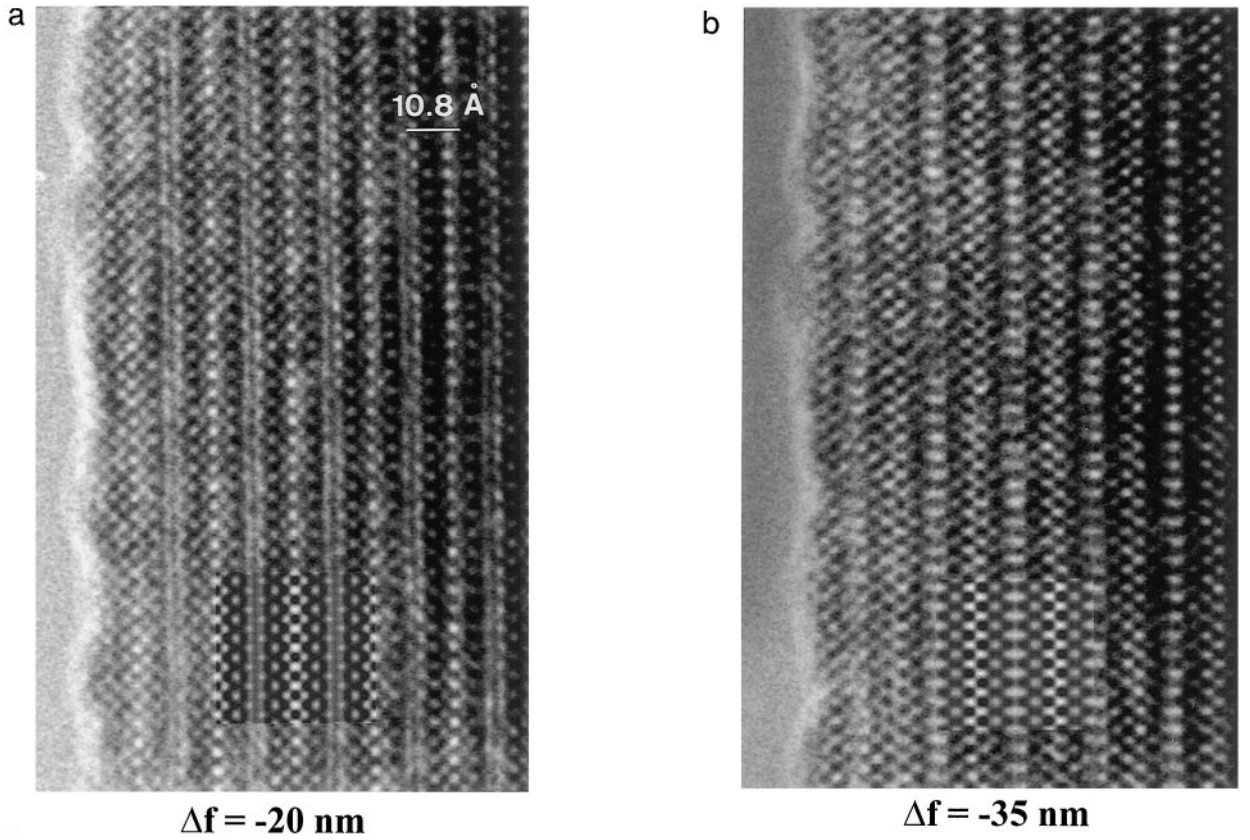

FIG. 14. Experimental and calculated [110] HREM images of $Li_2La_{2.25}(Nb_{1.25}Ti_{2.75})O_{13}$ ($n4$) with the proposed model for three defocus values and a thickness close to 2.3 nm: (a) $\Delta f = -20$ nm, (b) $\Delta f = -35$ nm, and (c) $\Delta f = -70$ nm.

the final phase, the shrinking of the cell builds octahedral sites for Li^+ ions, and every LiO_6 octahedron shares four edges in the (001) plane with four adjacent LiO_6 octahedra and the remaining eight edges are shared with the BO_6 octahedra.

In order to check our model, simulations have been performed in the space group $I4/mmm$ with the parameters and the atomic positions given in Table 3; the occupancy of the cationic sites is kept equal to those of the mother phase. Figure 14 shows $\langle 110 \rangle$ HREM images observed for a crystal of $Li_2La_{2.25}(Nb_{1.25}Ti_{2.75})O_{13}$ ($n4$) with the simulated images inserted. The best agreement is obtained for a small thickness (close to 2.3 nm). The good fit between observed and calculated images seems to confirm the model proposed.

CONCLUSION

In this work on lithium containing Ruddlesden–Popper phases in the series $Li_2La_x(Nb_{2n-3x}Ti_{3x-n})O_{3n+1}$ ($n = 2$, 3, and 4) and $Li_2Sr_{1.5}(Nb_{3-x}Fe_x)O_{10-x}$ ($n = 3$ and $x = 0$ or 0.115), we confirm by TEM (ED and HREM) the structures previously established in our laboratory from single crystal X-ray diffraction data and we observe an irreversible structural change induced during HREM imaging, occurring for the $n = 2$, 3, and 4 members in the series.

This transformation leads to a new structural type, described in the $I4/mmm$ space group, in which the perovskite layers are preserved but straightened and the c parameter is noticeably shortened. The main difference between the structure of mother phases and the common structural model that we propose for the final phases lies in the change in the Li^+ coordination which turns to octahedral from tetrahedral. To our knowledge, such a phase tansition has not been reported for other Ruddlesden–Popper phases containing bigger monovalent cations (Na^+, K^+, Rb^+, etc.); this fact emphasizes the particular role played by Li^+ ions which can adopt easily both tetrahedral and octahedral coordination.

We are now trying to induce externally the transition observed in the microscope. One of the explored ways consists in high pressure experiments, now in progress, according to the observed decrease in the cell volume.

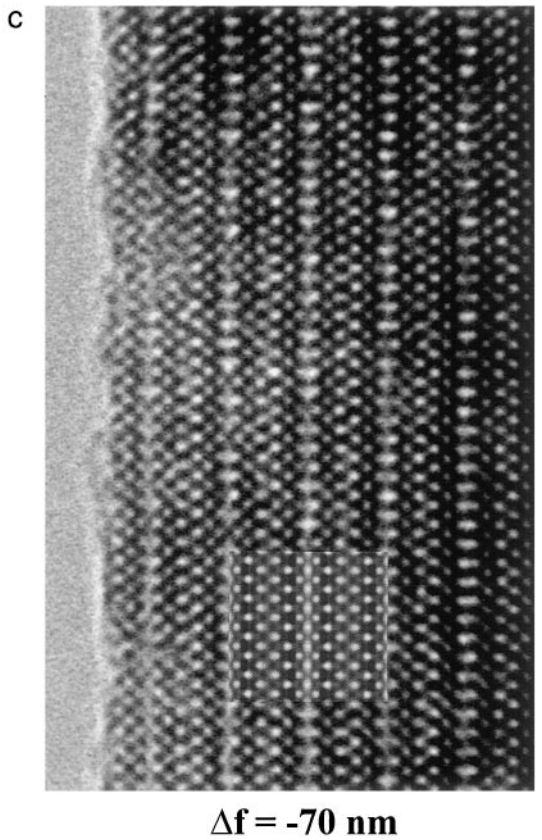

FIG. 14—*Continued*

ACKNOWLEDGMENT

The authors are very indebted to P. Noireaux (Centre de Transfert de Technologie du Mans) for electron beam tests. One of us (N.S.P.B.) thanks the Région des Pays de la Loire and the Centre National de La Recherche Scientifique for a postdoctoral fellowship.

REFERENCES

1. S. N. Ruddlesden and P. Popper, *Acta Crystallogr.* **10,** 538 (1957); **11,** 54 (1958).
2. M. Richard, L. Brohan, and M. Tournoux, *J. Solid State Chem.* **112,** 345 (1994).
3. M. Dion, M. Ganne, and M. Tournoux, *Mater. Res. Bull.* **16,** 1429 (1981).
4. M. Dion, M. Ganne, and M. Tournoux, *Rev. Chim. Miner.* **23,** 61 (1986).
5. A. J. Jacobson, J. W. Johnson, and J. T. Lewandowski, *Inorg. Chem.* **24,** 3727 (1985).
6. A. J. Jacobson, J. T. Lewandowski, and J. W. Johnson, *J. Less-Common Metals* **21,** 92 (1984).
7. A. J. Jacobson, J. W. Johnson, and J. T. Lewandowski, *Mater. Res. Bull.* **22,** 45 (1987).
8. K. Park and S-H. Byeon, *Bull. Korean Chem. Soc.* **17,** 168 (1996).
9. K. Toda, Y. Kameo, and M. Fujimoto, *J. Ceram. Soc. Japan Int. Edn.* **102,** 735 (1994).
10. S. Ikeda, A. Tanaka, M. Hara, J. N. Kondo, K. Maruya, and K. Domen, *Microporous Mater.* **9,** 253 (1997).
11. Y. Moritomo, A. Asamitsu, H. Kuwahara, and Y. Tokura, *Nature* **380,** 141 (1996).
12. R. Seshadri, C. Martin, M. Herien, B. Raveau, and C. N. R. Rao, *Chem. Mater.* **9,** 270 (1997).
13. P. D. Battle, M. A. Green, N. S. Laskey, J. E. Millburn, L. Murphy, M. J. Rosseinsky, S. P. Sullivan, and J. F. Vente, *Chem. Mater.* **9,** 552 (1997).
14. T. Williams, F. Lichtenberg, D. Widmer, J. G. Bednorz, and A. Reller, *J. Solid State Chem.* **103,** 375 (1993).
15. M. Hervieu, F. Studer, and B. Raveau, *J. Solid State Chem.* **22,** 273 (1977).
16. M. A. McCoy, R. W. Grimes, and W. E. Lee, *Phil. Mag. A*, **75** 833 (1997).
17. J. Sloan and R. J. D. Tilley, *Eur. J. Solid State Inorg. Chem.* **31,** 673 (1994).
18. D. Pasero and R. J. D. Tilley, *J. Solid State Chem.* **135,** 260 (1998).
19. F. Lichtenberg, T. Williams, A. Reller, D. Widmer, and J. G. Bednorz, *Z. Phys. B* **84,** 369 (1991).
20. M. P. Crosnier-Lopez, H. Duroy, and J. L. Fourquet, *Mat. Res. Bull.*, in press.
21. N. S. P. Bhuvanesh, M. P. Crosnier-Lopez, O. Bohnke, J. Emery, and J. L. Fourquet, *Chem. Mater.* **11,** 634 (1999).
22. P. A. Stadelman, *Ultramicroscopy* **21,** 131 (1987).
23. M. Sato, T. Jin, and H. Ueda, *Chem. Lett.* **161** (1994).
24. K. Toda, T. Honma, Z.-G. Ye, and M. Sato, *J. Alloys Comp.* **249,** 256 (1997).
25. K. Toda, T. Suzuki, and M. Sato, *Solid State Ionics* **93,** 177 (1997).
26. M. Sato, J. Abo, T. Jin, and M. Ohta, *Solid State Ionics* **51,** 85 (1992).
27. K. Toda and M. Sato, *J. Mater. Chem.* **6,** 1067 (1996).
28. T. R. Wagner, *J. Solid State Chem.* **91,** 189 (1991).
29. L. Nistor, G. Van Tendeloo, S. Amelinckx, V. Kahlenberg, and H. Böhm, *J. Solid State Chem.* **119,** 281 (1995).
30. Z. C. Kang and L. Eyring; *J. Solid State Chem.* **99,** 343 (1992).
31. M. Le Granvalet-Mancini, A. M. Marie, C. Roucau, M. Caldes, and L. Brohan, *Microsc. Microanal. Microstruct.* **8,** 203 (1997).
32. J. Y. Lee, J. S. Swinnea, H. Steinfink, W. M. Reiff, S. Pei, and J. D. Jorgensen, *J. Solid State Chem.* **103,** 1 (1993).
33. R. Genouel, C. Michel, N. Nguyen, F. Studer, M. Hervieu, and B. Raveau, *J. Solid State Chem.* **119,** 260 (1995).
34. R. Li, *Mater. Res. Bull.* **31,** 539 (1996).
35. M. Sato, J. Abo, T. Jin, and M. Ohta, *J. Alloys Comp.* **192,** 81 (1993).
36. J. L. Fourquet, P. A. Gillet, and A. Le Bail, *Mater. Res. Bull.* **24,** 1207 (1989).
37. K. H. Lii, C. H. Li, C. Y. Cheng, and S. L. Wang, *J. Solid State Chem.* **95,** 352 (1991).
38. R. Berger, P. Önnerud, Y. Laligant, and A. Le Bail, *J. Alloys Comp.* **190,** 295 (1993).
39. J. L. Fourquet, A. Le Bail, and P. A. Gillet, *Mater. Res. Bull.* **23,** 1163 (1988).
40. J. P. Attfield and G. Ferey, *J. Solid State Chem.* **80,** 112 (1989).